Performance comparison between different sparger plate orifice patterns: Hydrodynamic investigation using ultrafast X-ray tomography

Möller, F.; Seiler, T.; Lau, Y. M.; Weber, M.; Weber, M.; Hampel, U.; Schubert, M.;

Originally published:

February 2017

Chemical Engineering Journal 316(2017), 857-871

DOI: https://doi.org/10.1016/j.cej.2017.01.114

Perma-Link to Publication Repository of HZDR:

https://www.hzdr.de/publications/Publ-24742

Performance comparison between different sparger plate orifice patterns: Hydrodynamic investigation using ultrafast X-ray tomography

F. Möller[a,*], T. Seiler[a], Y. M. Lau[a], Mf. Weber[b], Mk. Weber[b], U. Hampel[a,c], M. Schubert[a]

[a]Insitute of Fluid Dynamics, Helmholtz-Zentrum Dresden-Rossendorf, Bautzner Landstr. 400, 01328 Dresden, Germany

[b]INEOS Phenol GmbH, Dechenstraße 3, 45966 Gladbeck, Germany

[c]AREVA Endowed Chair of Imaging Techniques in Energy and Process Engineering, Technische Universität Dresden, 01062 Dresden, Germany

*Corresponding author

Keywords

Bubble column, sparger performance, hydrodynamics, ultrafast X-ray tomography, flow evolution, gas-liquid mass transfer

Abstract

In this work, the effect of the sparger design on the hydrodynamic performance in a bubble column of 0.1 m ID downstream a single (coarse) and multi-orifice (fine) perforated plate sparger was studied using the ultrafast X-ray tomography. The liquid was kept in semi-batch mode and the superficial gas velocity was varied between 0.011 and 0.025 m s^{-1} to ensure non-jetting flow through the sparger holes. The effect of the orifice patterns on the hydrodynamic performance was evaluated through bubble size distribution (BSD), radial gas holdup profile and overall gas holdup as well as Sauter mean bubble diameter and magnitude of the interfacial area. To evaluate the sparger and bubble column performance, respectively, also the mass transfer was investigated. Due to the high turbulence induced by the large bubbles released from the coarse sparger, the equilibrium BSD was already reached at a dimensionless height of h/D = 1.0. However, average

bubble characteristics such as interfacial area and Sauter mean diameter were similar for both sparger types at a column height of $h/D \geq 7.0$. Based on a comprehensive hydrodynamic analysis, requirements for sparger refinement were derived depending on respective reaction rates, mixing properties, heat production and removal duty. Eventually, adapted correlations are proposed for radial holdup profile and Sauter mean diameter accounting for various plate refinements using liquids which inhibit coalesce of gas bubbles.

1 Introduction

Bubble column reactors (BCRs) are widely used as multiphase contactors in the chemical process industry. They find their application in oxidation, hydrogenation and bioprocesses, etc. [1–3]. BCRs are basically cylindrical vessels in which the liquid phase can either be kept in continuous or semi-batch mode and the gas phase is dispersed through a gas sparger, typically at the bottom of the column. Furthermore, since BCRs are constructed without moving parts, they are simple in design as well as maintenance. BCRs provide superior heat and mass transfer characteristics at comparably low energy input, which make them a competitive reactor type against conventional fixed bed or stirred tank reactors [4].

There are several sparger types which may be used to disperse the gas into the column. That is, perforated plates, ring- and pipe-type spargers, just to mention few ones. Many investigators have already pointed out that the design of the sparger for a specific column geometry as well as for a particular reaction system is very crucial for the overall bubble column performance [1,2,5,6]. Furthermore, designing a sparging device, which covers all hydrodynamic flow regimes, is very challenging, as maldistribution may occur for low superficial gas velocities [7,8]. The sparger type or the sparger holes, respectively, determines the initial bubble size at the bottom. The bubble size, in turn, determines the bubble rise velocity and with it the average gas holdup as well as its radial profile. Furthermore, it is well-known that the liquid velocity profile follows the gas holdup profile [9,10] and is decisive for the mixing behavior. Therefore, among others, the design of the

gas sparger determines the overall bubble column hydrodynamic and, thus, the bubble column performance [1,5,11].

A variety of studies have been carried out to evaluate the sparger performance and to draw conclusions about the optimal sparger designs (Table 1). Walke et al., (2012) [12] studied the influence of the pitch pattern (triangular and square) of perforated plate type spargers with various liquids using a high-speed camera. They found that the transition point between homogeneous and heterogeneous flow regime is independent of the hole size, which is contradictory to the investigations of [13–16], who reported on a strong effect of the sparger orifice diameter regardless of the opening area. Furthermore, the pattern type of the sparger showed an influence on the hydrodynamics in terms of overall gas holdup if water was used as the liquid phase. For spargers with a triangular pitch, coalescence at the orifice is promoted leading to lower gas holdups compared to the square pitch counterpart. For other liquid systems (see Table 1), however, the pitch type did not have any influence on the global hydrodynamic parameters [12]. In terms of effect of opening area on the overall gas holdup, Su and Heindel, (2005) [17] carried out a series of experiments with three perforated plate type spargers varying the number of holes only while keeping the hole size constant. They concluded that opening area has an effect at the transition region only, whereas the effect becomes negligible for homogeneous or heterogeneous conditions, respectively.

Other studies report on the bubble size distribution (BSD) using various distributors [7,10,15,18]. It is generally acknowledged that the BSD for perforated plates with small holes (e.g. d_o = 0.5 mm) is narrower for low velocities (approx. $u_g \leq 2$ cm s^{-1}) compared to larger orifice holes or single hole spargers, respectively. Furthermore, it has been concluded that the BSD mainly follows a log-normal distribution [7,19]. Mudde et al., (2009) [20] and Rabha et al., (2013) [21] mentioned that for a hole size of more than 1.6 mm bubbly flow condition for low superficial gas velocity can hardly be reached and, therefore, the churn-turbulent flow behavior is prevailing

[15,16]. With an increase of superficial gas velocity, the BSD widens for perforated plates due to coalescence phenomena. With increasing gas velocity, a bimodal distribution for perforated and porous plates was obtained, indicating a two-bubble class distribution [22].

Furthermore, higher gas holdups were measured for perforated plates compared to single orifice type spargers and spargers with larger orifice diameter, respectively [7,10,15,23,24]. This was also confirmed by CFD simulations by Li et al., (2009) [25]. With increasing gas velocity, the single hole sparger enters the jetting regime (roughly at $u_{g,o}$ = 40 cm s^{-1}), which induces a high turbulence at the orifice and the gas is introduced as a continuous jet. This, in turn, leads to even lower holdups due to coalescence [7,26]. With an increase of the velocity far beyond the transition to the churn-turbulent flow regime, e.g. u_g > 20 cm s^{-1}, the role of the sparger, however, becomes entirely insignificant [10,23]. If the liquid is contaminated with alcohols or salts, it has been found that the gas holdup increases due to inhibition of coalescence and the formation of smaller bubbles [15,27,28], which also delays the flow regime transition [15].

While the liquid phase mixing was found to be independent of orifice hole size of multi-hole spargers [10], the mixing time was found to enhance, if single hole spargers or asymmetrical spargers were used [25]. For the mixing time, Li et al., (2009) [25] concluded that with an asymmetrical arrangement of the holes, a better mixing is achieved because of larger circulation eddies formed in the lower part of the column, leading to higher turbulent intensities, which is also in line with the experimental investigations of other research articles [10,29,30]. Thorat et al., (1998) [28] and Veera and Joshi, (1999) [3] investigated the influence of the dispersion height on the sparger performance and revealed decreasing average gas holdups when using perforated plates with increasing dispersion height, whereas the single hole spargers showed an opposite trend. Here, with increasing h/D ratio the bubbles had sufficient time to break up and to form uniform smaller bubbles.

The influence of sparger type on mass transfer was investigated by Han and Al-Dahhan, (2006) [23]. They concluded that perforated plates with small holes (e.g. d_o = 0.5 mm) showed the highest $k_l a$ value, which was also due to a larger interfacial area. Furthermore, influence of sparger type on the mass transfer was only visible for low superficial gas velocities.

It is reported that the sparger effect is prevailing for one to two column diameters only [10,31], whereas the hydrodynamics is fully established for h/D > 5.0 or superficial gas velocities larger than 20 cm s^{-1} regardless of the sparger and its geometry [3,7,23,32].

To the best of the authors' knowledge, so far only two studies [5,33] suggested an approach for the selection of proper spargers considering various design parameters, e.g. pressure drop across the sparger. However, local hydrodynamics as well as flow patterns evolving from the sparger towards the hydrodynamic equilibrium zone are fully disregarded.

Therefore, the main objective of this work was to study the local flow structure and its evolution downstream two perforated plates with different spatial refinements, namely a single hole (coarse) and a multi-hole (fine) sparger with different hole size but identical total opening area. Furthermore, in order to determine the overall bubble column performance as a result of the evolving flow structure, the volumetric mass transfer coefficient was evaluated with a fast-responding oxygen needle probe. Therefore, ultrafast electron beam X-ray tomography and oxygen needle probes were applied to unveil the local and global hydrodynamics, i.e. gas holdup, radial holdup, bubble size distribution and Sauter mean diameter as well as the mass transfer coefficient, respectively. In particular, the work aimed on assessing the reasonable '*effort*' (in terms of design and construction) to provide fine initial distribution of the gas phase, since the manufacturing of a perforated plate with a larger number of small holes can be quite time consuming and costly [5,33].

Table 1: Summary of available sparger studies.

Authors	Column Specifications	Sparger Specifications	Measurement location (h/D)	Measurement technique	Superficial gas velocity range (cm s^{-1})	Investigated fluids
[12]	H_c = 1 m, H_{CL} = 0.92 m, D = 0.23 m	Two perforated plate type spargers (triangular and square pitch), d_o = 1 mm, A_o = 0.2%	-	High-speed camera, bed expansion	1.2 – 10.8	Air / deionized water, glycerin (50%), butanol (1.5%)
[7]	H_c = 1.5 m, H_{CL} = 0.56 m, D = 0.14 m	Single nozzle (d_o = 5.5 mm), perforated plate (d_o =3 mm), porous plate (d_{mean} = 0.6 mm)	2, 4, 5.6, 7.2	High-speed camera, bed expansion	3.25 – 10.8	Air / tap water and Air/tap water with addition of 5 wt% solids
[23]	H_D = 1.79 m, D = 0.162 m	Perforated plate (d_o = 1.32 mm, A_o = 1.09%), perforated plate (d_o =0 .5 mm, A_o = 0.156%), cross sparger (d_o = 2.54 mm, A_o = 0.1%)	0.7, 2.1, 2.8, 5.5, 8, 9.5	Optical fluorescence probes, bed expansion	0.5 – 60	Air / tap water
[26]	H_c = 2.5 m, D = 0.162 m	Three perforated plates (triangular pattern, d = 0.4, 0.5 and 1.25 mm, A_o = 0.1, 0.15 and 1%), single hole (d_o = 5.1 mm, A_o = 0.1%), cross sparger (d_o = 2.6mm, A_o = 0.1%), perforate plate (square pattern, d_o = 0.4 mm A_o = 0.15%)	2.1, 5.5, 9	Gamma-ray CT	2-30	Air / tap water
[10]	H_c = 2 m, D = 0.39 m	*'Tree'* type sparger (d_o = 0.5 mm and 3mm A_o = 2.2%), asymmetrical *'tree'* type sparger	0.13, 1.4, 2.7, 3.5	Needle probes, pressure taps, pitot tube	7-29	Air / water

[15]	H_c = 2 m, D = 0.127 m	Perforated plate (d_o = 0.5mm A_o = 0.19%), spider sparger (d_o = 2mm A_o = 0.89%)	7.87	Wire-mesh sensor, bed expansion	1-17	Air / deionized water, tap water, distilled water and 0.5% aqueous solution of butanol
[16]	H_c = 2 m, D = 0.1 m	Single nozzle (d_o = 5mm), perforated plate (d = 1mm), porous glass plate	8	LDA	0.6-15	Air / water
[3]	H_c = 3.2 m, H_D/D = 6, D = 0.385 m	Three perforated plate spargers (d_o = 1, 3, 0.8mm, A_o = 0.42%), two single hole spargers (d_o = 25, 87 mm A_o = 0.42, 5.4%)	0.259, 3, 5	Gamma-ray CT	6-29	Air / water
[34]	H_c = 6 m, D = 0.63 m	Ring sparger, perforated plate sparger, single hole sparger	2.14	Three-film electro diffusion electrode	2-9	Air / water with K_2SO_4 and solid loading varying from 0-10%
[29]	H_D/D = 1.5-3.5 m, D = 0.385 m	Single hole sparger (d_o = 25mm), multi orifice sparger (tree type sparger d_o = 3mm)	Bottom of column	Bed expansion, conductivity probes, concentration measurements	7-20	Air / tap water
[17]	H_c = 4 m, D = 0.152 m	Perforated plate type spargers (d_o = 1 mm, A_o = 0.57, 0.99, 2.14%)	6.56, 13.12	Pressure transducers	1 -17	Air / water – Rayon fiber

2 Experimental

In many bubble column applications the liquid phase mainly consists of mixtures containing inorganic and organic compounds. This is especially true for bio-reactors, which contain for example sugars, inorganic salts and metabolic products in the liquid phase reacting to alcohol and organic liquids [27,35]. Therefore, in this study, an air/deionized water system with traces of ethanol was used to mimic the typical non-coalescing behavior. The investigation of the sparger performance at low superficial gas velocities is very interesting, since a variety of processes are carried out at bubbly flow conditions [30]. For example, many bubble column bioreactors are operated in the homogeneous regime with non-jetting sparger flow in order to ensure the vitality of the enzymes since they mostly take part in bio-reactions.

2.1 Bubble column setup

A cylindrical bubble column of PMMA material with an inner diameter of D = 0.1 m, a height of H_c = 2 m and an unaerated liquid level of H_{CL} = 1.1 m was used for the tomographic study. The gas was supplied by the in-house gas supply and controlled via a mass flow controller (type OMEGA FMA-2608A, 0 L min^{-1} – 20 L min^{-1}). Experiments were performed at superficial gas velocities of 1.1, 1.8 and 2.5 cm s^{-1} to ensure gas hole velocities below roughly 30 m s^{-1} in order to avoid gas jetting [36,37]. Air/deionized water was used as fluid system and 20 ml of ethanol were added to inhibit coalescence as discussed above.

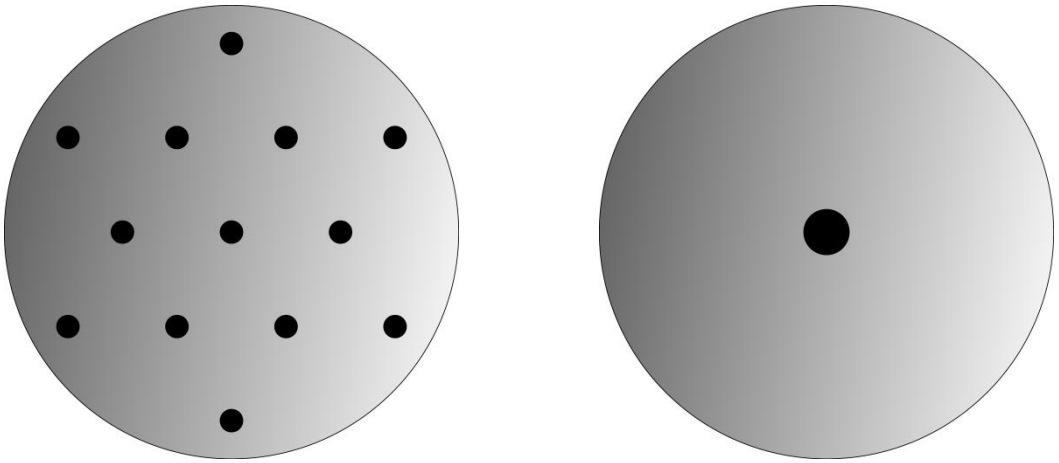

Figure 1: Perforated plate designs: left) 'fine' refinement with a hole size of d_o = 0.8 mm, right) 'coarse' refinement with a hole size of d_o = 2.9 mm (holes not to scale).

The two spargers which are depicted in Figure 1, have different hole refinements, namely, 13 holes (Figure 1 left) ('fine' refinement) with a diameter of d_o = 0.8 mm in a triangular pitch (24 mm, 60° layout) and a distributor with a centered hole (Figure 1 right) with d_o = 2.9 mm ('coarse' refinement). Both have the same opening area (A_o= 0.09%) in order to guarantee the same gas hole velocity.

2.2 X-ray computed tomography

For the investigation of the hydrodynamic as well as of the flow evolution in the column downstream the respective sparger, ultrafast electron beam X-ray computed tomography (CT) was used (Figure 2). It allows non-invasive cross-sectional imaging at very high spatio-temporal resolution [38]. The tomographic scanning principle is similar to conventional medical X-ray CT, however, to achieve high speed an electron beam is scanned across a circular target instead of rotating a massive X-ray tube around the object. The electron beam produces a rapidly rotating focal X-ray spot. X-rays are being attenuated in the column and their intensities are being measured by a fast ring-like X-ray detector with 432 pixels. A dual-plane arrangement allows to scan two slices with an axial distance of 11 mm simultaneously. The scanning speed in this study was 1000 Hz per plane, that is, tomography provides 1000 cross-sectional images per second.

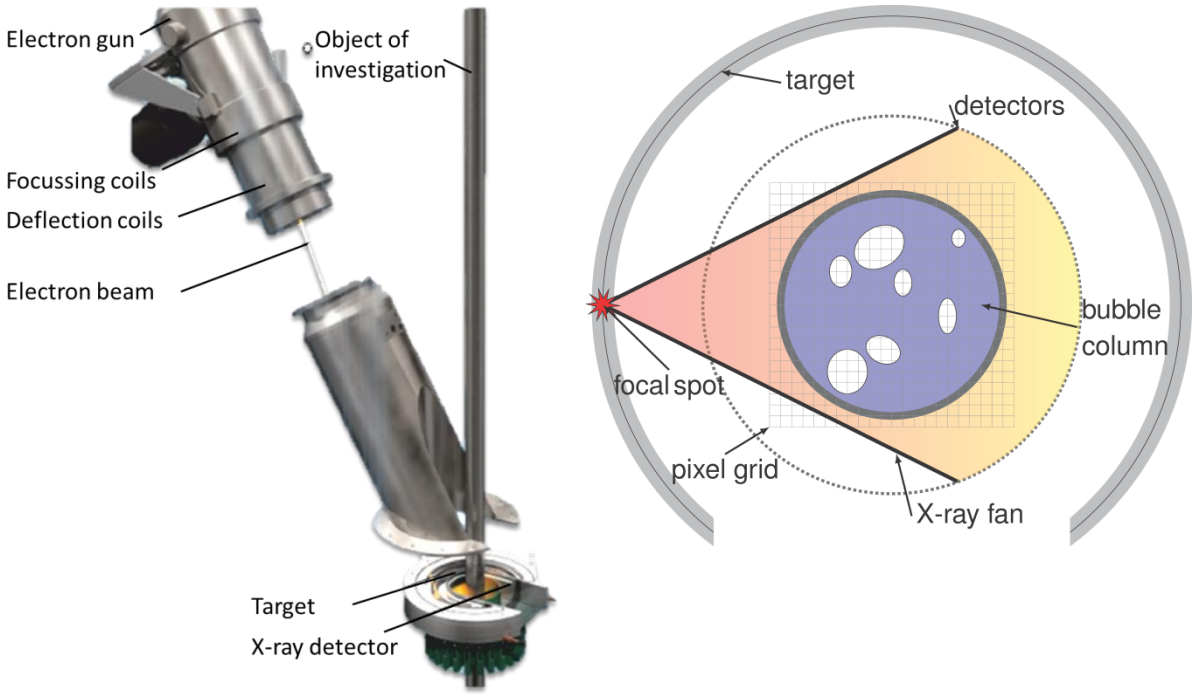

Figure 2: Measurement facility and cross- sectional area view of the scanning plane.

2.3 Tomography data post-processing

Figure 3 illustrates the data post-processing procedure. During the measurements, the recordings from the detector elements are stored in a data matrix. Subsequently, these data are being reconstructed by a filtered back-projection to obtain the reconstructed cross-sectional images. Then, normalizing and binarization procedures are applied to get binary images of the gas phase. First, the images are scaled between an empty and a fully liquid-filled BCR, which gives pixel values of 0 for pure gas, 1 for pure liquid, values in between for pixels with gas-liquid mixture and values >1 for the column wall. Eventually, all cross-sectional images are binarized and stacked to a 3D data set. Subsequently, algorithms for extraction of time-averaged gas holdups and radial gas holdup values are applied. Furthermore, the integral gas holdup was additionally measured by the level-swell method for comparison with the X-ray data. A circumferential averaging along the radius of the time-averaged holdup values was used to calculate the radial holdup profile. For further information regarding the post-processing, the reader is referred to Rabha et al., (2013) [21], Banowski et al., (2015) [39] and Lau et al., (2016) [40].

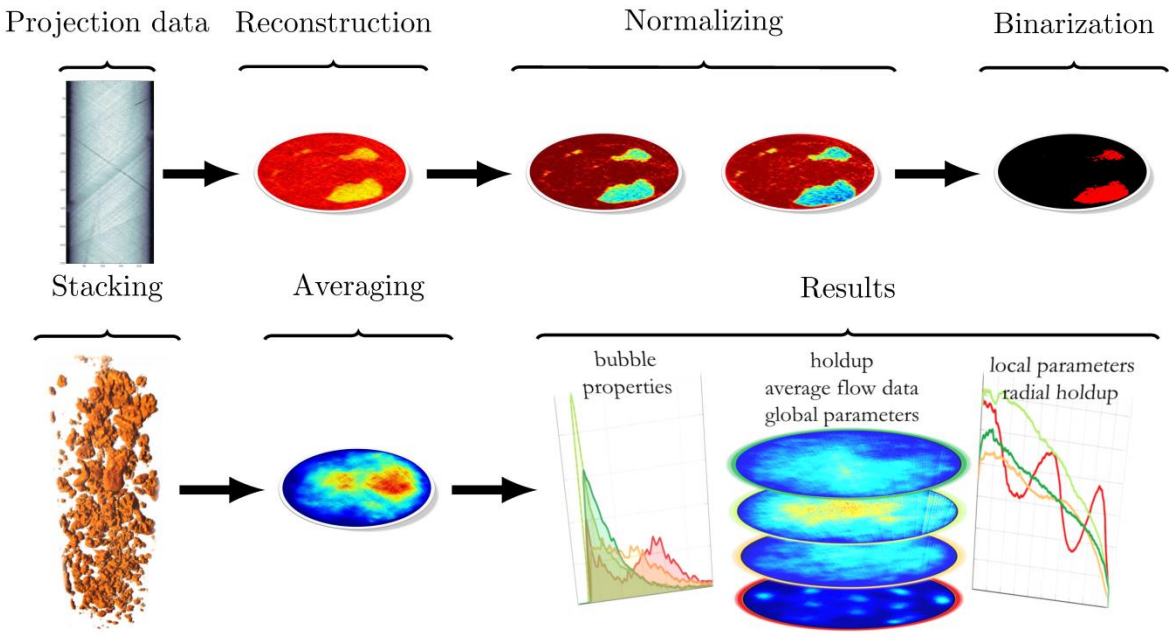

Figure 3: Flowchart of the data post-processing steps.

For the identification of individual bubbles from the stacked frames, it was predefined that the size of bubbles has to be greater than or equal to four pixels and should be visible in at least three consecutive frames [39]. Objects not meeting these requirements were withdrawn from further analysis in order to avoid noise artifacts.

The detected bubbles are shaped as clusters of volumetric voxels, where each voxel (see Figure 4) has a time step Δt as the z-axis. Therefore, the theoretical volume of one voxel is defined as $V_{\text{vox}} = px \cdot px \cdot \Delta t$.

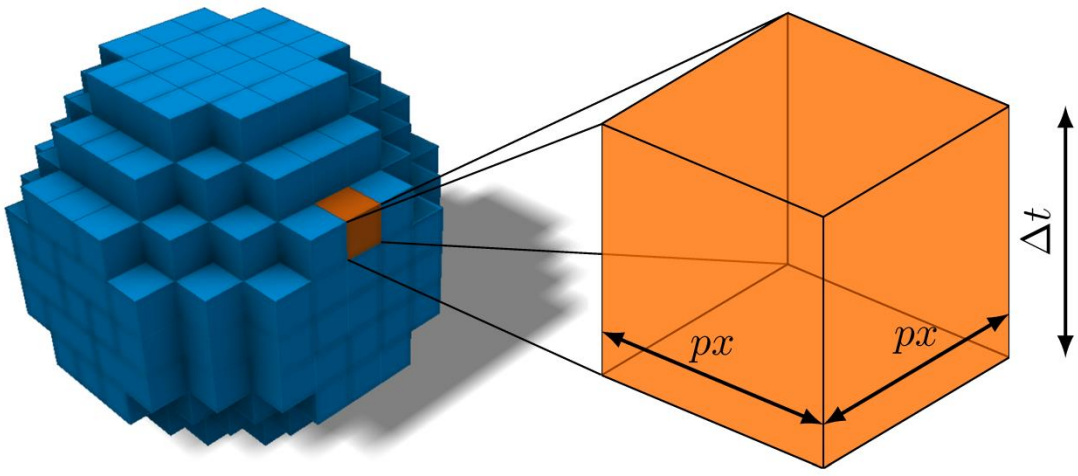

Figure 4: Voxel cluster representing a bubble (left) and respective voxel dimensions (right).

The voxel cluster of each bubble is the base for the calculation of the bubble size distribution. As a first step, the voxel cluster volume $\left(V_{\mathrm{b,v}} = n_{\mathrm{v}} \cdot V_{\mathrm{vox}}\right)$ of each detected bubble is calculated. For the determination of the real volume, the following formula is used:

$$V_{\mathrm{b}} = V_{\mathrm{b,v}} \cdot \left(0.5\ \frac{mm}{pix}\right)^2 \cdot \frac{u_{\mathrm{g}}}{\varepsilon_{\mathrm{g}}} \tag{1}$$

Here, $V_{\mathrm{b,v}}$ is the volume of the voxel, u_{g} describes the superficial gas velocity and ε_{g} depicts the cross-sectional holdup. Accordingly, $\frac{u_{\mathrm{g}}}{\varepsilon_{\mathrm{g}}}$ represents the bubble swarm velocity [1]. Since the images were reconstructed with an image resolution of 0.5 mm per pixel, the value $\left(0.5\ \frac{mm}{pix}\right)^2$ represents the conversion factor to convert the pixels into SI units.

With the assumption that the bubble is approximately spherical, the hydraulic diameter is calculated from the volume of an equivalent sphere as follows

$$d_{\mathrm{e}} = \left(\frac{6\,V_{\mathrm{b}}}{\pi}\right)^{\frac{1}{3}}. \tag{2}$$

The assumption of bubble sphericity was confirmed by visual observation.

After all these steps the BSD can be produced. There are several acknowledged ways to depict the BSD, namely, in a number density distribution [40,41] or in a volumetric distribution where the holdup fraction of a specific bubble class is divided by the diameter class $\left(\frac{\Delta\varepsilon_{\mathrm{g}}}{\Delta d_{\mathrm{e}}}\right)$ [15,42]. Both distributions can be found in Figure 5. On the left hand side the number density distribution of the coarse sparger at h/D = 1 and 1.1 cm s^{-1} is shown and on the right hand side the probability density function in dependence on the gas fraction per bin size for the fine sparger at h/D = 7 and 1.8 cm s^{-1} is shown. The probability density function on the right hand side can be seen as the volumetric gas holdup distribution per bubble diameter, which is basically the fraction of gas

holdup of a specific bubble size class. Here, it can be seen that the way of depiction has some influence on the conclusions. The number density function on the left side shows that lots of small bubbles (d_e < 5 mm) and less large bubbles (d_e > 5 mm) are found. For the volumetric BSD depiction, however, it can be seen that small and also large bubbles carry the majority amount of the overall volume. Furthermore, these distributions can be directly interrelated with each other applying the holdup fraction per bubble class diameter. For further discussion, the number density distribution will be used in order to illustrate the number of large and small bubbles along the bubble column height.

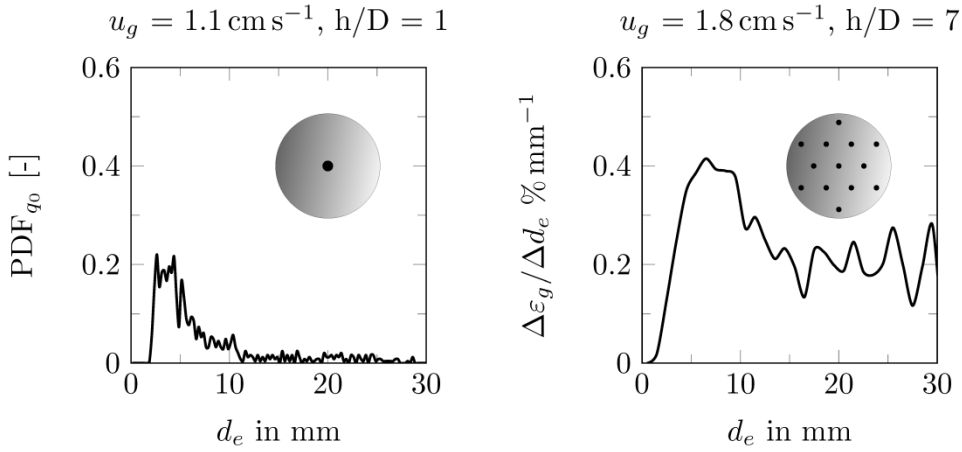

Figure 5: Comparison of bubble size distribution types.

2.4 Mass transfer measurements

For mass transfer measurements an oxygen needle probe (type UNISENCE, OX100) was applied. Since the overall volumetric mass transfer coefficient was determined, only one measurement height (h/D = 7.0) was used for inserting the probe.

In order to extract the volumetric mass transfer coefficient, the two most common models, namely, the continuous-stirred-tank-reactor (CSTR) model

$$\frac{dc_l}{dt} = \frac{k_l a}{\varepsilon_l}(c_l^* - c_l) \tag{3}$$

and the axial dispersion model (ADM)

$$\frac{dc_g}{dt} = D_{z,g}\frac{d^2c_g}{dz^2} - \frac{u_g}{\varepsilon_g}\frac{dc_g}{dz} - \frac{k_l a}{\varepsilon_g}\left(Hc_g - c_l\right)$$
$$\frac{dc_l}{dt} = D_{z,l}\frac{d^2c_l}{dz^2} + \frac{k_l a}{\varepsilon_l}\left(Hc_g - c_l\right) \quad (4)$$

approaches were used. Here, $D_{z,l}$ and $D_{z,g}$ denote the liquid and gas diffusion coefficient, respectively, H depicts the Henry's constant in dimensionless form, $k_l a$ depicts the volumetric mass transfer coefficient and the liquid and gas concentration are shown by c_g and c_l, respectively. Furthermore, the equilibrium concentration is denoted as c_l^*.

Liquid and gas dispersion coefficients needed for the ADM were taken from the correlations proposed by [43] and [44], respectively, which are suggested as very reliable ones in the literature [6], given by

$$D_{z,l} = 0.678 \cdot u_g^{0.3} D^{1.4} \quad (5)$$

$$D_{z,g} = 50 \cdot D^{1.5}\left(\frac{u_g}{\varepsilon_g}\right)^3. \quad (6)$$

Standard zero-gradient boundary conditions as proposed by Danckwerts, (1953) [45] were applied.

3 Results and discussion

In this section the experimental results, including global and local hydrodynamic parameters, such as bubble characteristics, gas holdup profiles and flow pattern will be discussed. In addition, the overall BCR performance is evaluated in terms of the overall volumetric mass transfer coefficient to complement the hydrodynamics.

3.1 Bubble size characteristics

The bubble size distribution (BSD) measured at several dimensionless heights (h/D) is shown in Figure 6, depicted as number probability density functions (PDF) counting the bubbles of a particular size passing the cross-sectional area of the X-ray scanner. The upper row shows the PDF obtained downstream the coarse sparger, whereas the lower row shows the PDF resulting from the fine sparger plate. A particular feature of ultrafast X-ray CT is to produce pseudo 3D

views stacked from sliced images gathered during one measurement. Thus, Figure 6 incorporates the respective pseudo 3D plots, where the z-axis denotes the time. The compilation shows virtually the flow axially evolving at various heights for the different superficial gas velocities.

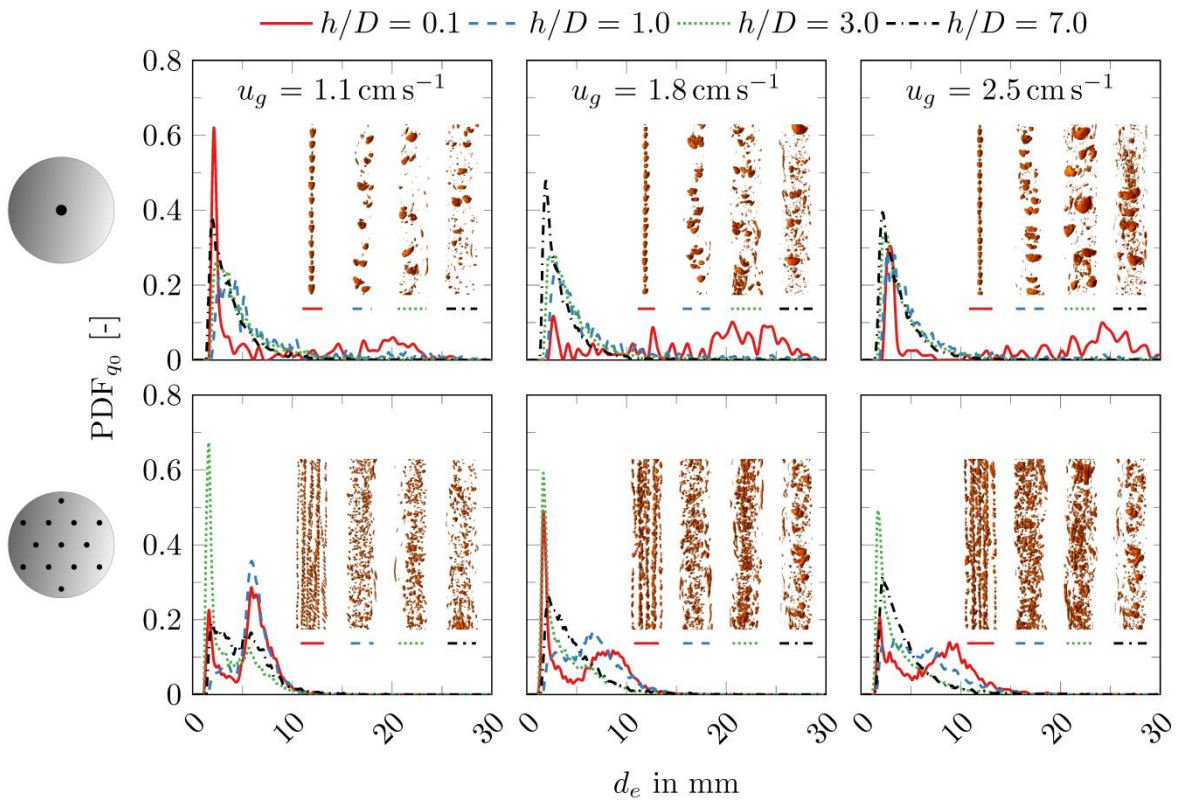

Figure 6: Number density distribution at several measurement heights depending on the superficial gas velocity (with inserted pseudo 3D views of the gas structure).

For the initial height (red solid line) of h/D = 0.1 a wide BSD can be found at low superficial gas velocity for the coarse sparger, which is characterized by a narrow peak at an equivalent diameter of approx. 3 mm as well as a long tail indicating bubbles of larger sizes up to 25 mm. It should be mentioned that the assumption of sphericity in case of larger bubbles might be inaccurate since rather ellipsoidal bubbles are produced at this size. Therefore, the bubble diameter, especially for larger bubbles, may overestimate Sauter mean diameter and specific surface area. With increasing superficial gas velocity, however, the narrow initial peak widens strongly due to the formation of larger bubbles at the orifice, which also confirms former findings [3,16,28,29]. At higher gas superficial velocities, there is even a tendency to produce a typical two-bubble class size

distribution at the orifice outlet [22] with peaks found at 3 mm (small bubble size class) and 25 mm (large bubble size class). Comparing the BSD at higher column position, however, only minor differences are found for respective gas superficial velocities. Due to the non-coalescing behavior of the liquid phase, the bubbles mainly undergo breakup events. Even the wide initial distributions at higher gas superficial velocities get rapidly narrow-shaped downstream the coarse sparger and an equilibrium BSD is reached almost after one column diameter. This is mainly driven by the high shear stress as well as high turbulence rates, which are generated [28] at the sparging zone, e.g. h/D < 2.0 [6,9,31,32], which in turn lead to high breakup rates. With further increase of the measurement height the impact of the bubble-induced turbulence decreases, which eventually leads to an equilibrium BSD.

The flow structure gives evidence that both sparger configurations ensure the non-jetting flow regime at the plate orifices. For the coarse sparger, small and large bubbles are alternatingly released confirming the bimodal BSD spectrum (two-bubble class size distribution) reported in Figure 6. For the fine sparger, the bubbles released at the center are larger compared to the bubbles relased near the column wall as shown in the pseudo 3D plots, which is even more significant at higher gas superficial velocities. Mainly bubble breakup events occur during the bubbles' rise. It can also be noted that less bubbles are found at the highest measurement position for the fine sparger. However, two-bubble class distribution with a comparably narrow BSD was observed regardless of the superficial gas velocity. Here, the initial BSD, which gets narrower at higher measurement positions, is mainly determined by the hole size. However, the BSD for the fine sparger requires at least three column diameters to reach an equilibrium BSD. At the lowest superficial gas velocity, the BSD for the fine sparger reaches its equilibrium not until seven column diameters indicating low shear and turbulence. Eventually, increasing superficial gas velocity and measurement height result in narrow BSDs for both sparger types (compare BSDs at u_g = 2.5 cm s^{-1} at h/D = 7.0). It is interesting to note that the BSD for the fine sparger amongst all investigated heights has the most narrow distribution at h/D = 3.0

indicating that the bubble will grow until h/D = 7.0 due to the reduction of the hydrostatic head. The major difference between both sparger types is that the turbulence near the coarse sparger is much higher compared to the fine sparger, which leads to higher breakup rates and to an earlier stabilization of the equilibrium BSD.

These conclusions are also confirmed by the Sauter mean diameter (SMD) as shown in Figure 7. The SMD is a widely accepted characteristic bubble size for bubble column reactors [46]. Furthermore, it is often applied to determine the interfacial area, which, in turn, is a very important parameter for the mass transfer prediction in the column design phase. The SMD can be calculated based on the BSD number density data according to

$$d_{32} = \frac{\sum_{i=1}^{m} n_i \cdot d_{i,e}^3}{\sum_{i=1}^{m} n_i \cdot d_{i,e}^2} \tag{7}$$

where n_i describes the ith bubble class and $d_{i,e}$ denotes the equivalent diameter in that class. For the coarse sparger, the SMD decreases exponentially with an increase of the measurement height. With increasing gas velocity, the generated SMD at the orifice outlet increases. Regardless of the velocity, the SMD approaches a similar value for all superficial gas velocities. However, an equilibrium SMD is not fully reached yet at the highest measurement position since breakup events are still occurring indicated by the further decrease of the SMD for h/D ranging from 3.0 to 7.0.

On the contrary, no clear trend can be observed from the SMD of the finer plate refinement. The SMD remains nearly constant for the lowest gas velocity. Increasing the gas velocity, shrinks the SMD little, which is probably due to a higher induced turbulence. Above three column diameters, the SMD starts to slightly increase again, which could be attributed to the decrease of the hydrostatic head eventually leading to a small expansion of the bubbles, respectively. This phenomenon was also visible for the course of the BSD: the BSD narrowed up to h/D = 3.0 and then widened up to h/D = 7.0 again (see Figure 6).

Although, the SMD for the coarse sparger is drastically higher near the sparger, in the fully developed flow region h/D > 5.0 [32] the SMD for both spargers turned out to be similar and the effect of the gas sparger disappears completely. Furthermore, it can be concluded that the superficial gas velocity has only very minor effects, which is also in line with the literature. For example Deckwer et al., (1978) [47] mentioned that the small decrease in the SMD with increasing superficial gas velocity can be attributed to an increase in turbulence. Hence, the turbulence within the gas-liquid flow field determines the SMD. It can be concluded that the SMD depends strongly on the column height when using a coarse sparger. For a fine sparger, however, the measurement height seems to be nearly negligible.

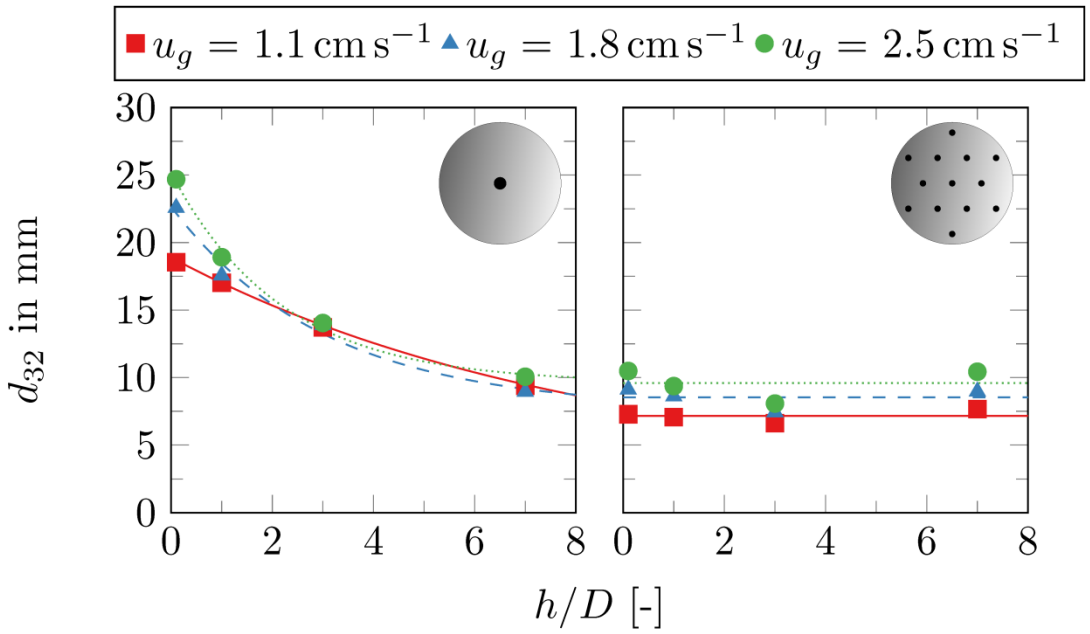

Figure 7: Sauter mean diameter vs. measurement height for coarse and fine sparger.

After the bubble properties are studied, the global and local holdups are investigated, since the holdup is influenced by the number and size of the bubbles. Indeed, it is known, that smaller bubbles generate larger holdups and vice versa for larger bubbles [15]. Therefore, in the next section the influence of bubble characteristics and sizes, respectively, are compared with the holdup properties.

3.2 Gas holdup

The cross-sectional holdup distribution (pattern) evolving along the measurement height is depicted in Figure 8. In addition, the corresponding cross-sectionally averaged gas holdup data are shown in Figure 9. The gas holdup pattern at the orifice of the coarse sparger is almost the same for all three superficial gas velocities, which is also quantitatively confirmed by Figure 9. With increasing height the holdup increases and reaches a plateau at an axial height of around seven column diameters. As evident from Figure 8 at least three column diameters are required to spread the gas-liquid dispersion towards the column wall downstream the coarse sparger. With increasing superficial gas velocity, the average gas holdup increases reasonably and the influence of the column height on the cross-sectional holdup distribution becomes more evident. Downstream the fine sparger, however, the gas phase is evenly distributed from the holes and covers the whole cross-section already at an axial height of one column diameter. Above three column diameters, the holdup tends to stay rather constant over the measurement height as shown in Figure 8. Compared to the coarse sparger, the finer refinement results in a much more uniform gas distribution in the column's cross-section after around one column diameter regardless of the superficial gas velocity.

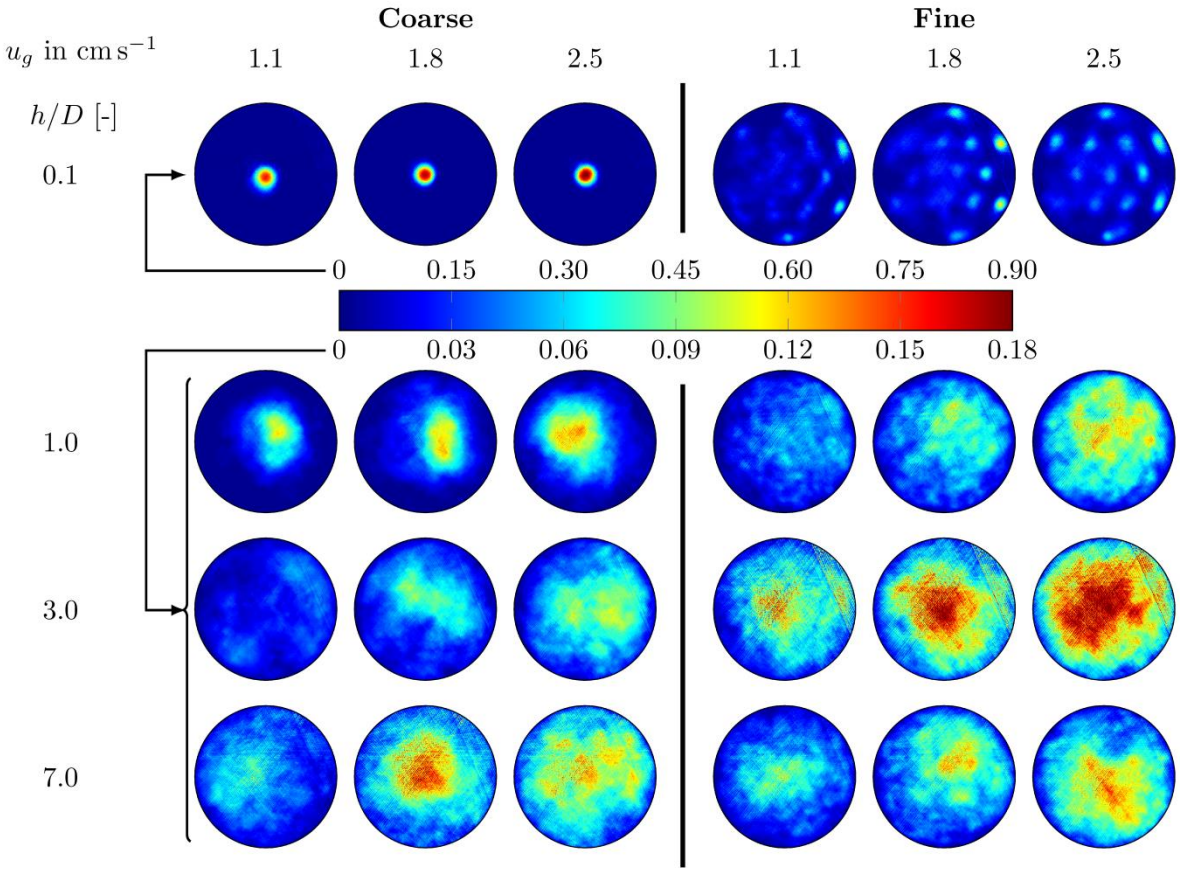

Figure 8: Axial evolution of the cross-sectional gas holdup distribution for coarse and fine sparger for different superficial gas velocities.

For the coarse sparger, the average gas holdup at the orifice outlet is similar for all three velocities and increases linearly towards h/D = 3.0 until the slope flattens towards the uppermost measurement height, being in the more developed flow (see Figure 9). Since the holdup continues rising with increasing measurement height, yet no conclusion can be drawn on the fully developed flow regime. The reason for the larger increase in holdup with increasing measurement height observed for the coarse sparger is that the larger bubbles generated at the orifice outlet, immediately start to break, while coalescence is inhibited. After around three column diameters, the initially high breakup frequency decreases remarkably. For the fine sparger, however, a small drop of the gas holdup is noticed at the highest measurement position at the velocities of 1.8 and 2.5 cm s^{-1}, which is due to the reduction of the hydrostatic head, leading to an increase in the

bubble size, which, in turn, results in higher bubble rise velocities and, thus, lower cross-sectional holdups.

Other researchers pointed out that for perforated plate type spargers the fully developed flow occurs after approximately three column diameters [48]. It is widely acknowledged that the sparger region will typically cover one column diameter [31], which is also in line with the measurements for the fine sparger. At the orifice outlet, the holdup is slightly higher compared to the other heights. After around one column diameter measurement height, the holdup remains constant, which could not be confirmed for the coarse sparger as discussed above.

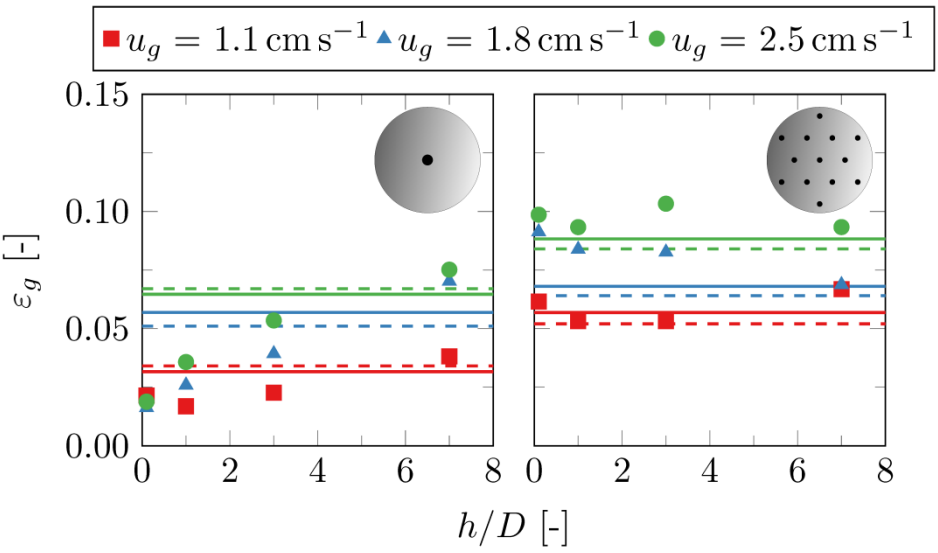

Figure 9: Axial evolution of cross-sectional average gas holdup for coarse and fine sparger (solid line: integral holdup from CT according to Eq. 8, $\bar{\varepsilon}_{g,CT}$, dashed line: integral holdup from level swell method, $\bar{\varepsilon}_{g,LS}$).

In addition, the integral gas holdup was calculated based on the computer tomography (CT) measurements taken at various heights according to the following equation:

$$\bar{\varepsilon}_{g,CT} = \frac{\sum_{i=1}^{4} \varepsilon_{g,i} z_i}{\sum_{i=1}^{4} z_i}. \tag{8}$$

In Equation 8, $\bar{\varepsilon}_{g,CT}$ describes the integral gas holdup determined by the ultrafast X-ray CT, $\varepsilon_{g,i}$ denotes the cross-sectional average holdup per i^{th} measurement position and z_i represents the distance from the sparger at the i^{th} measurement position.

The values for the integral holdup agree well with the one measured via the widely applied level swell (LS) method [1,15,49]. Both values are shown in Figure 9 by horizontal lines. The fine sparger produces constantly higher gas holdups compared to the coarse sparger because smaller bubbles are produced, hence, the bubble velocity is small resulting in higher gas holdups.

The corresponding time-averaged radial gas holdup profiles are depicted in Figure 10 with the coarse sparger in the upper and the fine sparger in the lower row. The bubble release from each hole can be clearly seen directly above the sparger by major profile peaks with gas holdup values up to 90% for the coarse sparger. The pronounced gas holdup gradients cause high circulating velocities and large circulation eddies in the sparging region [28], which coincides with large bubble-induced turbulence due to the shearing effects generated by large bubbles at the sparger orifice [7]. After one column diameter, the profile gets already smoothed.

The sinusoidal radial gas holdup profile measured near the fine sparger mirrors the holes distribution of the cross-sectional area. Similar profiles are observed at higher gas velocities, however, with a parabolic base function. The smooth parabolic radial profile, widely reported in the literature [50–52], is mostly developed after one column diameter, where only the slope changes.

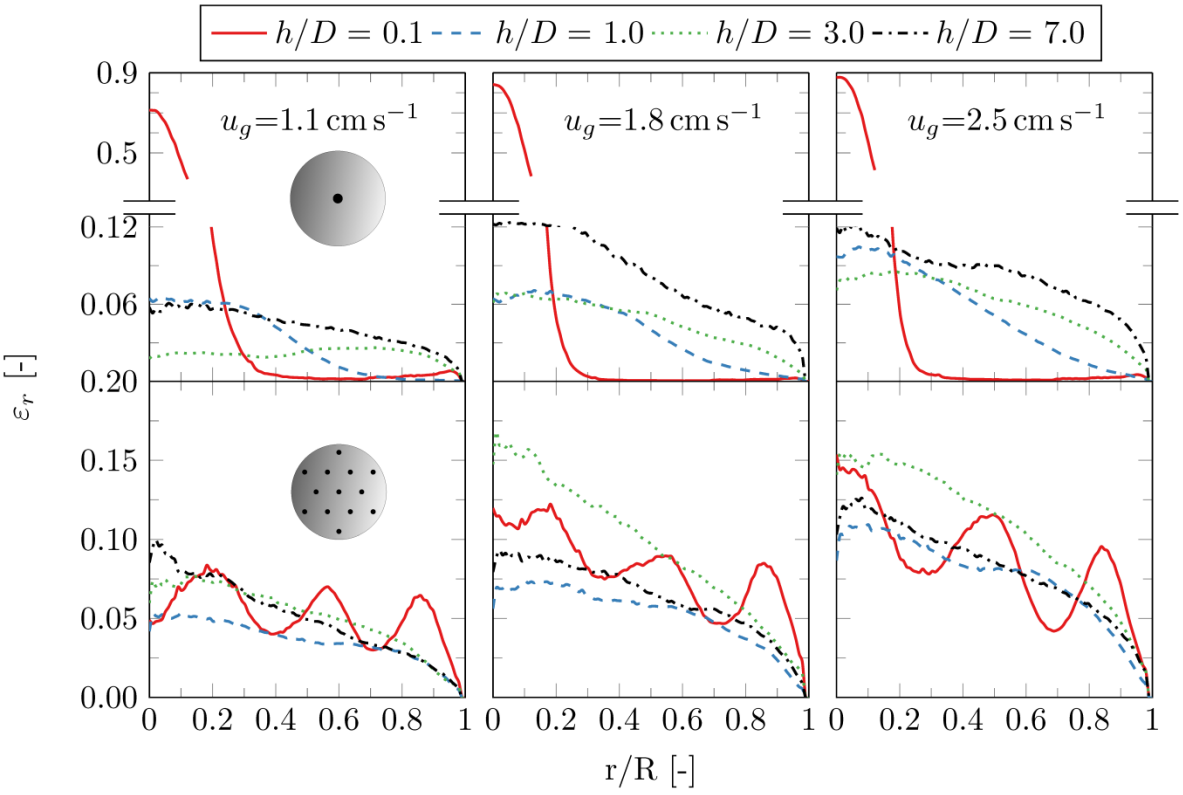

Figure 10: Average radial gas holdup evolution over the measurement height for both sparger types.

3.3 Interfacial area

In order to get a better insight into the performance of the sparger types with respect to mass transfer, the interfacial area will be subsequently determined. Since the interfacial area is dependent on the gas holdup as well as on the Sauter mean diameter, these two main BCR design parameters are taken into account. Although, the interfacial area can only be measured within a certain range of accuracy, the Sauter mean diameter can be applied to approximate the area assuming spherical-shaped bubbles according to

$$a = \frac{6 \cdot \varepsilon_g}{d_{32}}. \tag{9}$$

Sphericity can be fairly assumed since the applied superficial gas velocities are comparably low and the addition of small amount of ethanol hinders coalescence, however, for the coarse sparger this assumption will lead to some overestimation errors, as discussed before. In Figure 11 the interfacial area for all velocities and the two sparger types is depicted along the column height,

which shows – in particular for the coarse sparger – an opposite trend compared to the SMD shown in Figure 3, since, the small bubbles at higher column height provide a larger interfacial area. It can be seen that the interfacial area is almost a linear function of the height. For the fine sparger the interfacial area remains almost constant along the bubble column height. Comparing the interfacial area of both spargers at the top height, however, they almost equalize regardless of the initial BSD produced by the spargers. For the fine sparger, the interfacial area was slightly different for all the velocities, apart from the last measurement height. Here, the velocity seems to be negligible in terms of interfacial area. For the coarse sparger, however, velocity has a stronger impact. For u_g = 1.1 cm s^{-1} the interfacial area is always smaller comparing to the other two velocities. This might be due to the fact that the cross-sectional holdup decreased for decreasing superficial gas velocities. Therefore, the induced turbulence is lower, which, in turn, lowers the breakup rate and subsequently the cross-sectional holdup. Equation 9 supports the findings for SMD (Figure 7) and gas holdup (Figure 9). For the coarse sparger the gas holdup increases with increasing measurement height while the SMD decreases. Therefore, the trend of the interfacial area is increasing. For the fine sparger, however, both, the gas holdup and the SMD remain nearly constant along the measurement height similar to the interfacial area.

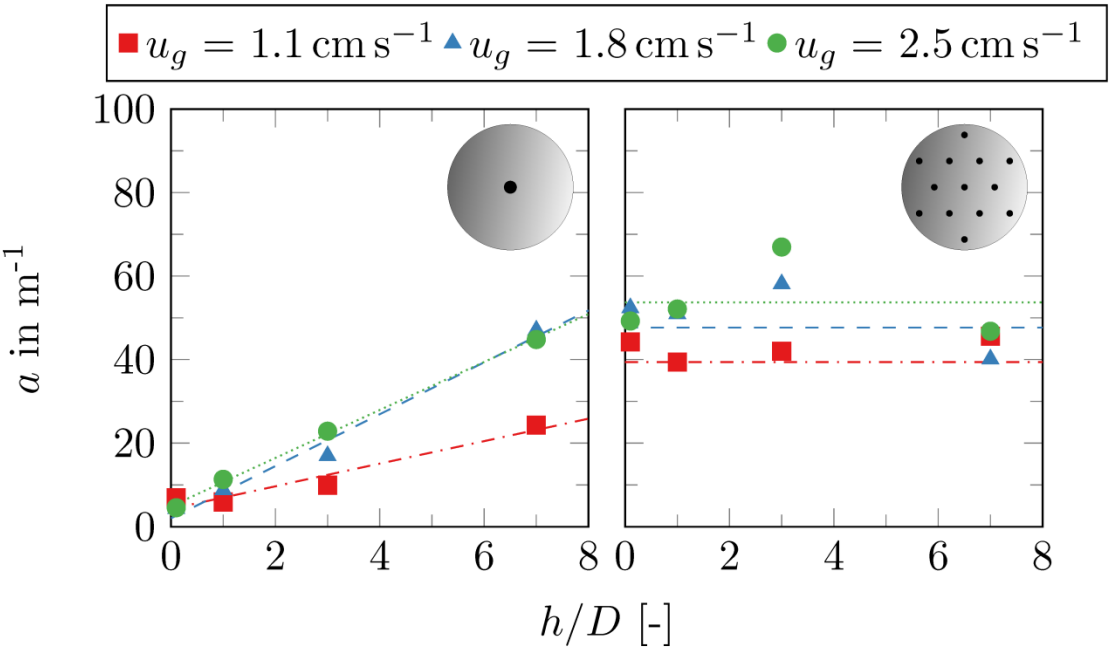

Figure 11: Interfacial area vs. measurement height for coarse and fine sparger. The lines indicated the trend of the specific surface evolution over the dimensionless height.

Therefore, the average gas holdup is higher from the finer sparger compared to the coarse sparger, which, in turn, implies that smaller bubbles are created at the fine sparger leading to higher interfacial areas and therefore, providing a higher mass transfer coefficient [46,49]. For fast reactions, having a high mass transfer or large interfacial areas would be advantageous, respectively [1]. These finding will be further discussed below in terms of mass transfer to determine the overall bubble column performance and efficiency.

3.4 Mass transfer

For the extraction of the volumetric mass transfer coefficient, two models were used, namely the axial dispersion model (ADM) and the continuous-stirred-tank-reactor (CSTR) model (see Section 2.4). In Figure 12, the match between the two models with the measurements are shown. The dimensionless concentration on the y axis is calculated as $C_{\mathrm{norm}} = \frac{c_l - c_0}{c_\infty - c_0}$. Both models agree well with the measurements as shown in Figure 12. Since, the ADM requires values for the axial liquid and gas dispersions, it was decided to use the CSTR model for the extraction of the

volumetric mass transfer coefficient for both spargers in order to be consistent and to avoid further errors through the use of correlations.

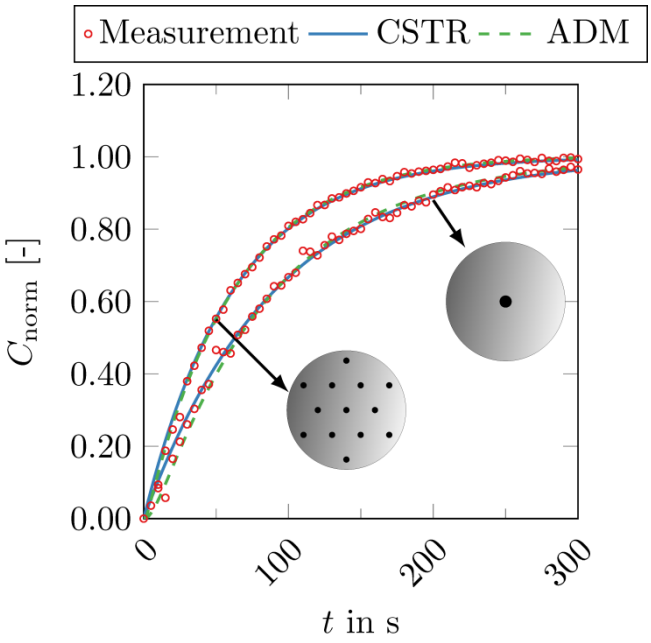

Figure 12: Comparison of CSTR and ADM for determination of the overall volumetric mass transfer coefficient.

In Figure 13 (left axis) the volumetric mass transfer coefficient $k_l a$ is depicted for both spargers. As previous results already indicated, the mass transfer coefficient depends directly on the hydrodynamic behavior. As already discussed in Section 3.2, the overall gas holdup is higher for the fine sparger (see Figure 8), which pushes the mass transfer coefficient. The volumetric mass transfer coefficient increases for both spargers with the gas velocity, however, for the fine sparger the increase is steeper compared to the coarse sparger indicating a better overall performance. Therefore, it can be concluded that the $k_l a$ value increases with an increase of the gas holdup and the interfacial area, as is has been proven by Nedeltchev, (2016) [53].

Since data for the interfacial area are available (see Section 3.3), one can extract the value of the liquid-side mass transfer coefficient, k_l, in order to get some insights into the turbulent behavior of the bubble column (see Figure 13 right axis). Here, the k_l value is increasing with increasing velocity for both sparger types, thus indicating higher turbulence. For the first velocity, the coarse

sparger has a higher turbulence compared to the fine sparger, which is attributed to the fact that the interfacial area was not as high as for the fine sparger. This was also confirmed by the measured BSD for the fine sparger at the lowest superficial gas velocity, which showed an equilibrium BSD after h/D = 7.0 (see Figure 5) indicating low turbulence rates.

The shrinkage of the SMD with increasing superficial gas velocity (see Fig. 6) is due to higher turbulence within the gas/liquid flow field, which is now also confirmed by the k_l value, which increases with increasing gas velocity. For the coarse sparger, the k_l value does not follow such clear trend, however, it confirms the results from the SMD (see Figure 7) at h/D = 7.0, showing that the superficial gas velocity has a negligible effect at that specific height since the k_l values are somewhat of a similar order for all investigated velocities.

With increasing velocity, the increasing k_l value of the fine sparger indicates also a more turbulent field compared to the coarse sparger. However, considering measured BSD and SMD, the coarse sparger showed pronounced turbulence in the sparger region. For the overall turbulence, the fine sparger shows larger values compared to the coarse sparger, indicating that the overall performance of the fine sparger is better compared to the coarse sparger.

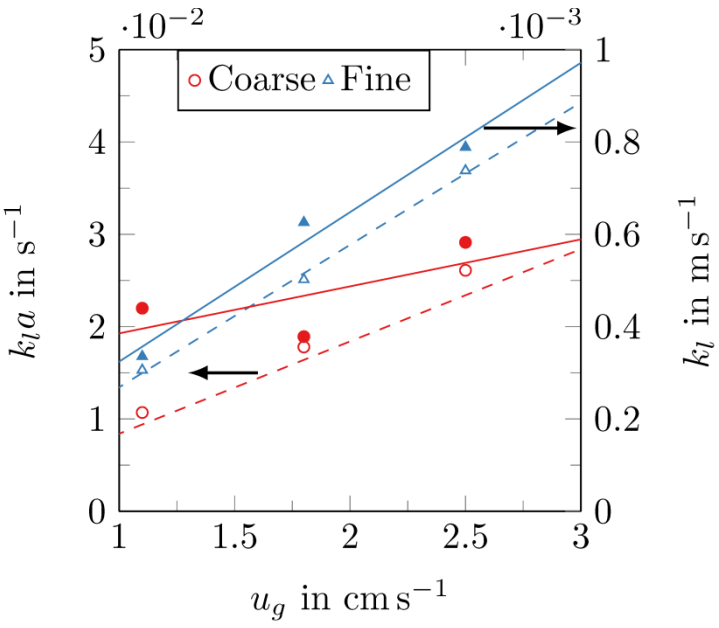

Figure 13: Overall volumetric mass transfer coefficient (axis on the left and hollow symbols) and k_l (axis on the right and filled symbols) for coarse and fine sparger. The dashed curves show the trend for the $k_l a$ value and the solid lines show the trend for the k_l value.

4 Literature comparison

4.1 Comparison of the radial holdup profile

The radial holdup profile is a very important design parameter for BCRs, since its shape and magnitude determine the phase interactions, hence, the turbulence as well as the gas and liquid velocity profile and corresponding circulation parameters. Subsequently, only the fully developed gas holdup profile at h/D = 7.0 is considered. Several correlations have been proposed in the literature to predict the radial gas holdup as summarized in Table 2. The equations developed by Luo and Svendsen, (1991) [50] and Wu et al., (2001) [52] are of similar structure considering only different coefficients c and n as well as different positions of the fitting parameter c in the equation. While Wu et al., (2001) considered n to account for fluid properties, Luo and Svendsen, (1991) [50] suggested a constant. Schweitzer et al., (2001) [51] developed a correlation which has a parabolic shape with three fitting constants independent on flow characterisitics and liquid and gas properties.

Figure 14 compares predicted and measured radial gas holdup profiles. Here, only the radial holdup profile for the superficial gas velocities of 1.1 and 2.5 cm s^{-1} are shown for the sake of clarity. It can be seen that none of the proposed correlations predicts the radial holdup profile satisfactorily. In particular, the higher holdup data obtained in the column center are not met properly.

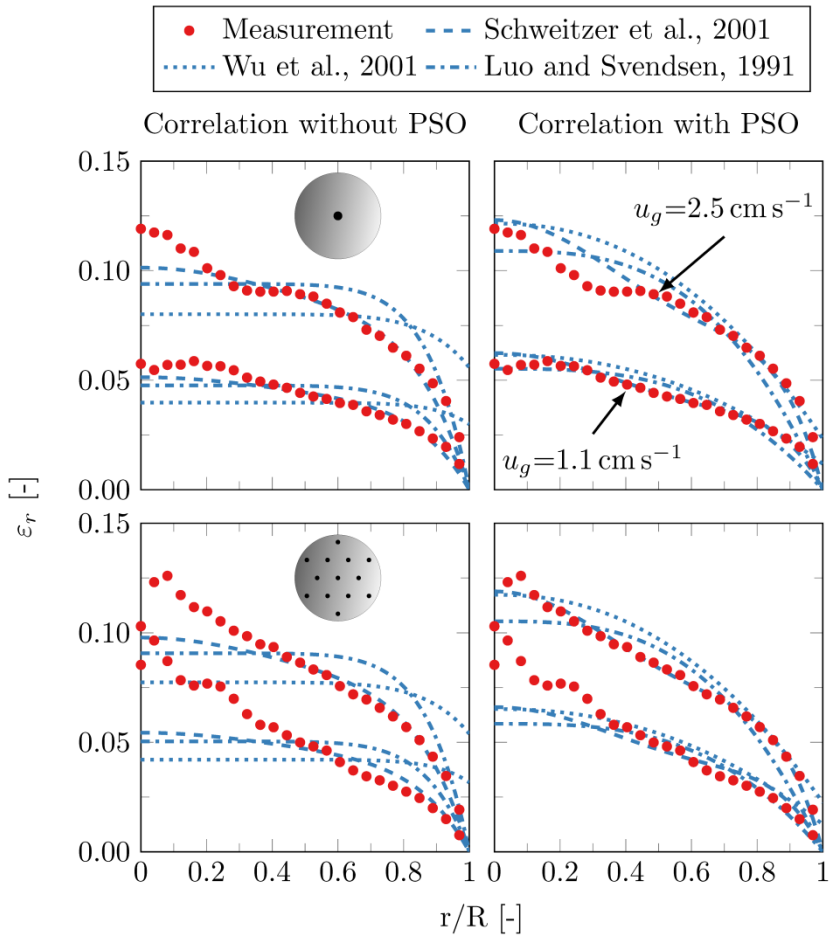

Figure 14: Comparison of radial holdup distributions from available and modified correlations with the measurements. The left column shows the proposed correlations from the original article and the right column shows the modified correlation with the aid of PSO.

The deviations between the applied correlations and the measurement data were calculated applying the average absolute relative error (AARE), which is defined as follows:

$$\mathrm{AARE} = \frac{1}{N}\sum_{i=1}^{n}\frac{\left|y_{\mathrm{p,i}} - y_{\mathrm{m,i}}\right|}{y_{\mathrm{m,i}}}. \tag{10}$$

Here, N is the number of considered radial points, $y_{\mathrm{p,i}}$ is the predicted and $y_{\mathrm{m,i}}$ the measured value, respectively. The determined deviations are always larger than roughly 50% (see Table 2). This large error results from the narrow column, which is expected to show significant wall effects. Contrary, the considered correlations [50–52] were mostly developed for column diameters larger than 0.15 m, where wall effect can be excluded.

Using the particle swarm optimization (PSO) approach [54], new coefficients c and n, summarized in Table 2, were determined being valid for both spargers at all measured velocities. Applying the PSO (see Figure 14), the correlations from Schweitzer et al., (2001) [51] and Wu et al., (2001) [52] provide the least deviation of approx. 30%.

Table 2: Used correlation for the prediction of the radial gas holdup and comparison between the originally proposed and fitted parameters using PSO.

Reference work	**Correlation**		**Coefficients proposed in the original work**	AARE **[-]**	**Coefficients from PSO**	AARE **PSO [-]**
[50]	$\varepsilon_{g,r} = \overline{\varepsilon_g}\left(\frac{n+2}{n+2-2c}\right)\left[1-\left(\frac{r}{R}\right)^n\right]$	(11)	$c = 1$, $n = 8$	0.6607	$c = 3.1$, $n = 0.8$	0.5604
[52]	$\varepsilon_{g,r} = \overline{\varepsilon_g}\left(\frac{n+2}{n+2-2c}\right)\left[1-c\left(\frac{r}{R}\right)^n\right]$	(12)	$c = 4.32 \cdot 10^{-2} Re_g^{0.2492}$, $n = 2.188 \cdot 10^3 Re_g^{-0.598} Fr_g^{0.146} Mo_l^{-0.004}$	1.0323	$n = 2.24$ $c = 0.81$	0.3698
[51]	$\frac{\varepsilon_{g,r}}{\overline{\varepsilon_g}} = -a_1\left(\left(\frac{r}{R}\right)^6 - 1\right) + a_2\left(\left(\frac{r}{R}\right)^4 - 1\right) - a_3\left(\left(\frac{r}{R}\right)^2 - 1\right)$	(13)	$a_1 = -1.638$, $a_2 = 1.228$, $a_3 = 0.939$	0.466	$a_1 = -3.374$, $a_2 = 4.599$, $a_3 = -2.868$	0.2824

4.2 Comparison of the Sauter mean diameter

Various well-known correlations (summarized in Table 3) were used for comparison with the measured Sauter mean diameter in the fully-developed flow, i.e. uppermost measurement height. Correlations from [55–60] have been selected for the comparison since they cover a wide range of experimental conditions and were developed based on data from various liquids. Among all the correlations, the one from Akita and Yoshida, (1974) [46] is used, which is widely recommended and used in the literature, respectively [6]. There is quite a numerous amount of researchers (e.g. [58] for further correlations of this type see [27]) proposing correlations with the following proportionality: $d_{32} \sim (6b/\pi)^{\frac{1}{3}} g^5 G^{\frac{2}{5}}$. Here, only the coefficient b is adapted to the respective experimental data. Winterson, (1994) [60] even claimed that the Sauter mean diameter depends only on the column diameter. Akita and Yoshida, (1974) [46] and Jamialahmadi et al., (2001) [57] studied the effect of several sparger types as well as a variety of liquid properties on the Sauter mean diameter. Akita and Yoshida, (1974) [46] determined the most influential parameters via dimension analysis. [57] Jamialahmadi et al., (2001) [57] used the same dimensionless groups to describe their experimental results. Furthermore, they made their dimensionless groups dependent on the orifice diameter, d_o, which was disregarded by Akita and Yoshida, (1974) [46].

Table 3: Comparison of various correlations for the prediction of the Sauter mean diameter from the originally proposed and fitted parameters using PSO.

Reference work	Correlation		Coefficients proposed in the original work	AARE [-]	Coefficients from the PSO	AARE PSO [-]
[55] [58]	$d_{32} = \left(b \cdot \frac{G^{\frac{6}{5}}}{g^{\frac{3}{5}}} \cdot \frac{6}{\pi} \right)^{\frac{1}{3}}$	(14)	$b = 1.378$ $b = 0.976$	0.1053 0.0978	$b = 0.07$	7.0753e-4
[56]	$d_{32} = \left[\left(\frac{b_1 d_o \sigma_l}{\rho_l g} \right)^{\frac{4}{3}} + \left(\frac{b_2 \nu_l G}{\pi g} \right) + \left(\frac{b_3 G^2}{4\pi g} \right)^{\frac{4}{5}} \right]^{\frac{1}{4}}$	(15)	$b_1 = 6, b_2 = 81$ $b_3 = 135$	0.1004	$b_1 = 30.4, \quad b_2 = 262.5, b_3 = 27.8$	0.0037
[60]	$d_{32} = bD$	(16)	$b = 0.04$	0.2186	$b = 0.0767$	0.0344
[46]	$\frac{d_{32}}{D} = 26 \cdot \left(\frac{D^2 g \rho_l}{\sigma_l} \right)^{-0.5} \left(\frac{g D^3}{\nu^2} \right)^{-0.12} \left(\frac{u_g}{\sqrt{gD}} \right)^{-0.12}$	(17)		0.0488		
[59]	$d_{32} = \sqrt[3]{\frac{3\sigma_l d_o}{\rho_l g} + \sqrt{\left(\frac{3\sigma_l d_o}{\rho_l g} \right)^2 + \frac{k_m G^2 d_o}{g}}}$	(18)	$k_m = 10, 13.9, 15$	0.0933		
[57]	$\frac{d_{32}}{d_o} = \left[\frac{5.0}{Bo_{d_o}^{1.08}} + \frac{9.261 Fr^{0.36}}{Ga^{0.39}} + 2.147 Fr^{0.51} \right]^{\frac{1}{3}}$	(19)		0.0883		

Figure 15 highlights the deviation between measurements and predictions by means of a parity plot. It can be seen that most of the correlations contradict the measurements. Only the prediction of Akita and Yoshida, (1974) [46] is within a reasonable deviation for both distributors, since they developed their correlation using experimental data obtained from various single hole and perforated plate type sparger with various fluids.

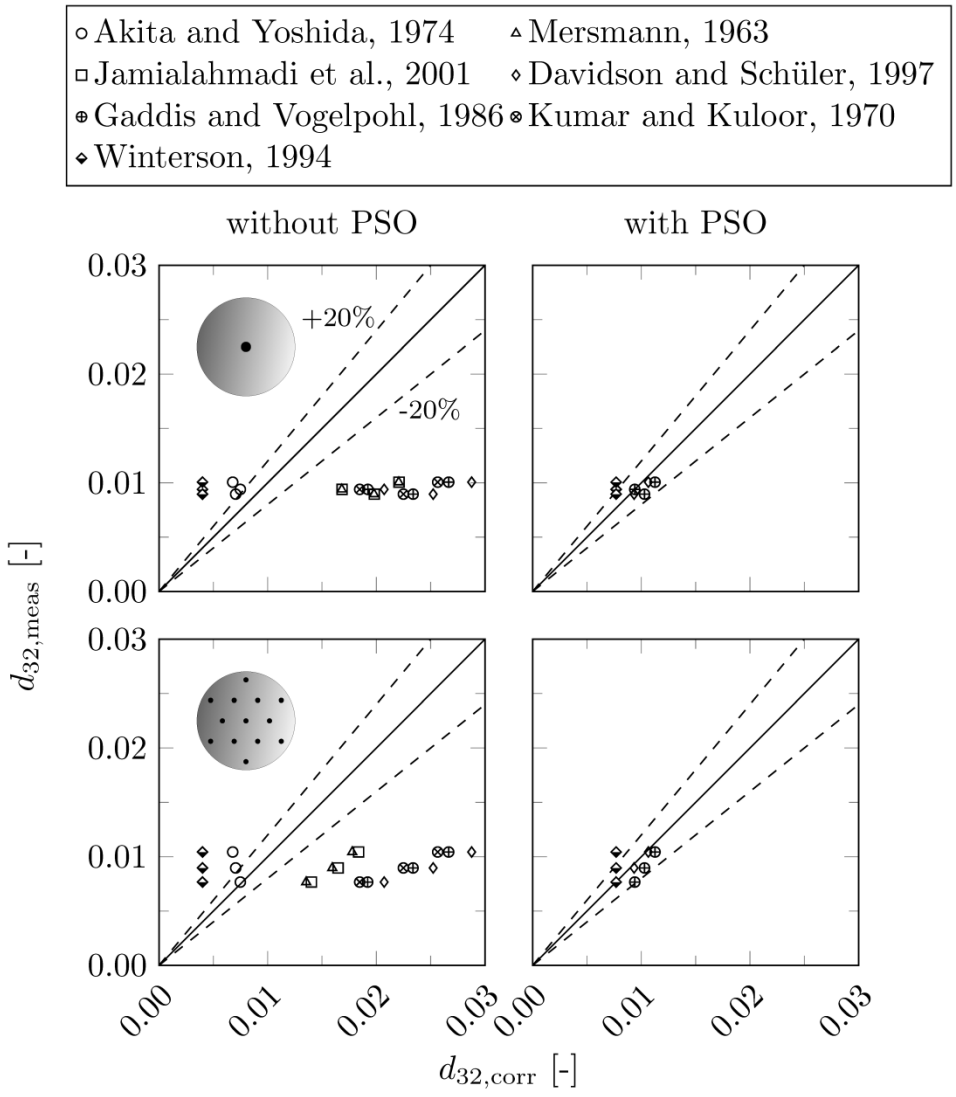

Figure 15: Comparison of the measured Sauter mean diameter with the one calculated using literature correlations.

Applying the PSO on the correlations of Davidson and Schüler (1997) [55], Gaddis and Vogelpohl, (1986) [56] and Winterson, (1994) [60], new values for the fitting parameters were determined, which allow predicting the Sauter mean diameter within a deviation of less than 20%. The modified parameters can also be found in Table 3 together with the values of the AARE.

4.3 Comparison of the average gas holdup

It is known that the addition of surfactants or, in actual fact, traces of alcohols increases the overall gas holdup compared to pure water systems. These additives cause the formation of smaller bubbles and suppress coalescence, thus, primarily breakup occurs [27]. In Table 4 the correlations of two research groups, who studied the overall gas holdup in bubble columns are summarized, since their studies covered a wide range of liquid properties as well as various sparger types.

Table 4: Correlations used for predicting the overall gas holdup.

Author	Correlation		AARE [-]
[49]	$\frac{\varepsilon_g}{(1-\varepsilon_g)^4} = 0.2\left(\frac{gD_C^2\rho_l}{\sigma_l}\right)^{\frac{1}{8}}\left(\frac{gD_c^3}{\nu_l^2}\right)^{\frac{1}{12}}\left(\frac{u_g}{\sqrt{gD_c}}\right)$	(20)	0.1944
[61]	$\frac{\varepsilon_g}{(1-\varepsilon_g)^4} = 0.672\left(\frac{u_g\mu_l}{\sigma_l}\right)^{0.578}\left(\frac{\mu_l^4 g}{\rho_l\sigma_l^3}\right)^{-0.131}\left(\frac{\rho_g}{\rho_l}\right)^{0.062}\left(\frac{\mu_g}{\mu_l}\right)^{0.107}$	(21)	0.1130

Figure 16 shows the prediction of the gas holdup in comparison with the measurements by means of parity plots. For the coarse sparger, it is suggested to use the correlation proposed by Hikita et al., (1980) [61], whereas for the fine sparger both correlations either slightly over- or underpredict the measurements, respectively. Nevertheless, both correlations are applicable, as they are within a maximum error range of 20 % and showing a fair agreement with the measurement carried out in this study.

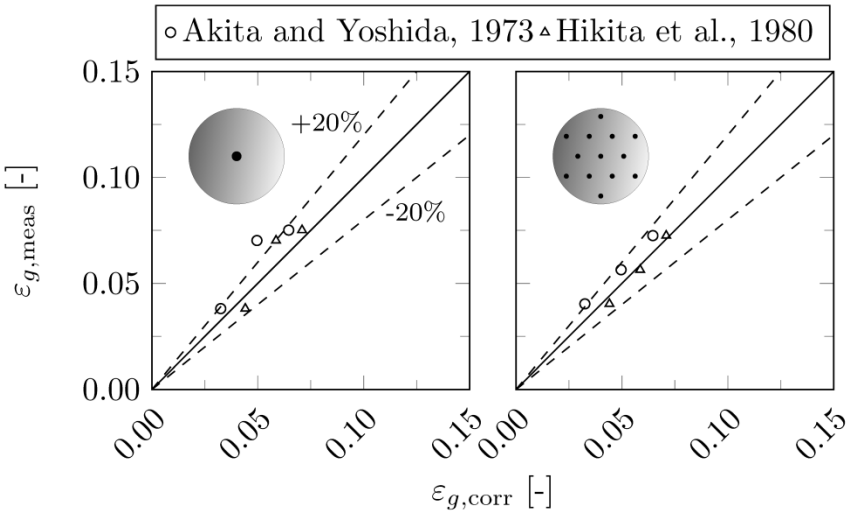

Figure 16: Parity plot for the overall holdup prediction.

5 Conclusions

In this study the effect of sparger type, namely, coarse and fine sparger plate refinement, was studied at low superficial velocities to ensure non-jetting conditions. Four different column heights have been evaluated ranging between $0.1 \leq h/D \leq 7.0$ to detect the flow evolution using ultrafast X-ray tomography.

The fine sparger shows a better hydrodynamic behavior, producing finer bubbles, which, in turn, lead to higher gas holdup and a larger interfacial area, which was also confirmed by higher mass transfer coefficients. Furthermore, the finer sparger resulted in a more uniform distribution of the bubbles across the reactors' cross-sectional area, which improves the efficiency of the gas flow rate on the mass transfer coefficient. Furthermore, experiments revealed that $k_l a$ increases with the enhancement of gas holdup as well as gas-liquid interfacial area. Therefore, in particular reactions, which are mass transfer limited, or fast reactions will be enhanced using finer spargers. Nevertheless, a coarse sparger could be beneficial for example in shallow bubble columns (h/D<2-5) [30] to enhance the mixing in the distributor zone. Furthermore, large eddies are created in the sparger zone leading to high liquid circulation velocities, which in turn, induce high turbulence reaching the equilibrium bubble size nearly after one column diameter due to the high

breakup rates. The coarse sparger could be used for slow reactions as the mixing is enhanced and the reaction is not dependent on the mass transfer. Furthermore, [62] mentioned that shallow bubble columns are often used in the industry where the gas phase has the purpose of cooling. Here, short gas residence times can be advantageous.

Eventually, it can be concluded that the selection of the sparger types in terms of refinement depends in particular on the available column dimensions as well as on the chemical reaction carried out in the BCR.

Acknowledgement

The authors gratefully acknowledge the European Research Council (ERC StG, No. 307360) as well as Helmholtz Association (within the frame of the Helmholtz Energy Alliance "Energy Efficient Chemical Multiphase Processes", HEA-E0004) for financial support.

Nomenclature

Acronyms

ADM Axial dispersion model

AARE Absolute average relative error

BCR Bubble column reactor

BSD Bubble size distribution

CSTR Continuous stirred tank reactor

CT Computed tomography

LDA Laser-Doppler-Anemometry

PDF Probability density function

PSO Particle swarm optimization

SMD Sauter mean diameter

Roman Symbols

A_o Opening area %

a Interfacial area m^{-1}

a_1, a_2, a_3 Fitting parameters [-]

b_i Fitting parameters [-]

c_i Concentration of i^{th} phase (i = gas, liquid) mol m^3

C_{norm} Normalized concentration [-] $C_{norm} = \frac{C_l - C_0}{C_\infty - C_0}$

d_{32} Sauter mean diameter m

$d_{32,corr}$ Sauter mean diameter from correlation m

$d_{32,meas}$ Sauter mean diameter from measurement m

d_e Equivalent m

$d_{i,e}$ Equivalent bubble diameter in i^{th} class m

d_{mean} Mean pore diameter of sintered plate type spargers m

d_o Orifice diameter m

D Column diameter m

$D_{z,i}$ Dispersion coefficient for i^{th} phase (i = gas, liquid) $m^2 s^{-1}$

e Error [-]

G Volumetric Flowrate $m^3 s^{-1}$

g Earth acceleration m s^{-2}

H Henry constant [-]

H_c Column height m

H_{CL} Clear liquid height m

H_{D} Dispersed liquid height m

h/D Dimensionless distance from the sparger [-]

k_{l} Gas/Liquid resistance m s^{-1}

$k_{\mathrm{l}}a$ Volumetric mass transfer coefficient s^{-1}

k_{m} Friction factor [-]

N Number of measurement points

n_i Number of bubble in i^{th} class [-]

n, c Fitting parameters [-]

px Pixel

q_0 Number distribution [-]

$\frac{r}{R}$ Dimensionless radius [-]

t Time [s]

u_{g} Superficial gas velocity cm s^{-1}

$u_{\mathrm{g,o}}$ Hole superficial gas velocity m s^{-1}

V_{b} Bubble volume m^3

$V_{\mathrm{b,v}}$ Pixel bubble volume $pixel^3$

V_{vox} Voxel volume [$pixel^3$]

y_{m} Measurement quantity for AARE calculation

y_{p} Predicted quantity for AARE calculation

z_{i} Axial position [-]

Greek symbols

Δd_{e} Equivalent diameter within one bubble class m

$\Delta \varepsilon_{\mathrm{g}}$ Gas holdup difference within one bubble class [-]

Δt Time difference in dependence on the measurement frequency s

$\varepsilon_{g,corr}$ Overall gas holdup from correlation [-]

$\bar{\varepsilon}_{g,i}$ Overal gas holdup depending on measurement technique (I = CT, LS) [-]

$\varepsilon_{g,meas}$ Overall gas holdup from measurement [-]

$\varepsilon_{g,r}$ Radial Gas holdup [-]

ε_l Liquid holdup [-]

ν_l Kinematic liquid viscosity $m^2 s^{-1}$

μ_i Liquid or gas dynamic viscosity Pa s

ρ_i Gas or Liquid density kg m^{-3}

σ_l Surface tension N m^{-1}

Dimensionless numbers

$Bo_{d_0} = \frac{\rho_l g d_0^2}{\sigma_l}$ Bond number depending on the orifice diameter

$Fr_g = \frac{u_g^2}{g D_c}$ Froude Number

$Fr_{d_0} = \frac{u g_{d_0}^2}{d_0^2 g}$ Froude number depending on the orifice diameter

$Ga_{d_0} = \frac{\rho_l^2 d_0^3 g}{\mu_l^2}$ Galileo number depending on the orifice diameter

$Mo_l = \frac{g \mu_l^4}{(\rho_l - \rho_g)\sigma_l^3}$ Morton number

$Re_G = \frac{D_c u_g (\rho_l - \rho_g)}{\mu_l}$ Reynolds number

Bibliography

[1] W.D. Deckwer, *Bubble Column Reactors*, (John Wiley & Sons Inc: 1992).

[2] N. Kantarci, F. Borak, K.O. Ulgen, Bubble column reactors, Process Biochemistry 40 (2005) 2263–2283.

[3] U.P. Veera, J.B. Joshi, Measurement of Gas Hold-Up Profiles by Gamma Ray Tomography, Chemical Engineering Research and Design 77 (1999) 303–317.

[4] W.-D. Deckwer, A. Schumpe, Improved tools for bubble column reactor design and scale-up, Chemical Engineering Science 48 (1993) 889–911.

[5] A.V. Kulkarni, J.B. Joshi, Design and selection of sparger for bubble column reactor. Part I: Performance of different spargers, Chemical Engineering Research and Design 89 (2011) 1972–1985.

[6] Y.T. Shah, B.G. Kelkar, S.P. Godbole, W.-D. Deckwer, Design parameters estimations for bubble column reactors, AIChE Journal 28 (1982) 353–379.

[7] R. Lau, W.S.B. Sim, R. Mo, Effect of gas distributor on hydrodynamics in shallow bubble column reactors, The Canadian Journal of Chemical Engineering 87 (2009) 847–854.

[8] S. Nedeltchev, T. Donath, S.S. Rabha, U. Hampel, M. Schubert, New Evidence for the Mixing Length Concept in a Narrow Bubble Column Operated in the Transition Regime, Journal of Chemical Engineering of Japan 47 (2014) 722–729.

[9] P. Gupta, B. Ong, M.H. Al-Dahhan, M.P. Dudukovic, B.A. Toseland, Hydrodynamics of churn turbulent bubble columns: gas-liquid recirculation and mechanistic modeling, Catalysis Today 64 (2001) 253–269.

[10] D.D. McClure, C. Wang, J.M. Kavanagh, D.F. Fletcher, G.W. Barton, Experimental investigation into the impact of sparger design on bubble columns at high superficial velocities, Chemical Engineering Research and Design 106 (2016) 205–213.

[11] W. Freedman, J.F. Davidson, Hold-up and Liquid Circulation In Bubble Columns, Transactions of the Institution of Chemical Engineers and the Chemical Engineer 47 (1969) T251–T262.

[12] S.M. Walke, V.S. Sathe, Study on the Gas Holdup of Triangular Pitch and Square Pitch Sparger Geometry in Bubble Column, International Journal of Fluid Mechanics Research 39 (2012) 85–97.

[13] H. Chaumat, A.M. Billet, H. Delmas, Axial and radial investigation of hydrodynamics in a bubble column; Influence of fluids flow rates and sparger type, International Journal of Chemical Reactor Engineering 4 (2006) (A25) 1–22.

[14] J. Drahoš, J. Zahradník, M. Fialová, F. Bradka, Identification and modelling of liquid flow structures in bubble column reactors, Chemical Engineering Science 47 (1992) 3313–3320.

[15] S. Sharaf, M. Zednikova, M.C. Ruzicka, B.J. Azzopardi, Global and local hydrodynamics of bubble columns - Effect of gas distributor, Chemical Engineering Journal 288 (2016) 489–504.

[16] C. Vial, R. Lainé, S. Poncin, N. Midoux, G. Wild, Influence of gas distribution and regime transitions on liquid velocity and turbulence in a 3-D bubble column, Chemical Engineering Science 56 (2001) 1085–1093.

[17] X. Su, T.J. Heindel, Effect of Perforated Plate Open Area on Gas Holdup in Rayon Fiber Suspensions, Journal of Fluids Engineering 12 (2005) 816–823.

[18] V.V. Buwa, V.V. Ranade, Dynamics of gas/liquid flow in a rectangular bubble column: experiments and single/multi-group CFD simulations, Chemical Engineering Science 57 (2002) 4715–4736.

[19] M.O.O. Kagumba, M.H. Al-Dahhan, Impact of Internals Size and Configuration on Bubble Dynamics in Bubble Columns for Alternative Clean Fuels Production, Industrial & Engineering Chemistry Research 54 (2015) 1359–1372.

[20] R.F. Mudde, W.K. Harteveld, H.E.A. van den Akker, Uniform Flow in Bubble Columns, Industrial & Engineering Chemistry Research 48 (2009) 148–158.

[21] S.S. Rabha, M. Schubert, M. Wagner, D. Lucas, U. Hampel, Bubble size and radial gas hold-up distributions in a slurry bubble column using ultrafast electron beam X-ray tomography, AIChE Journal 59 (2013) 1709–1722.

[22] Y.T. Shah, S. Joseph, D.N. Smith, J.A. Ruether, Two-bubble class model for churn turbulent bubble-column reactor, Industrial & Engineering Chemistry Process Design and Development 24 (1985) 1096–1104.

[23] L. Han, M.H. Al-Dahhan, Gas-liquid mass transfer in a high pressure bubble column reactor with different sparger designs, Chemical Engineering Science 62 (2007) 131–139.

[24] B.C. Ong, Experimental Investigation of Bubble Column Hydrodynamics - Effect of Elevated Pressure and Superficial Gas Velocity, PhD Thesis Washington University in St. Louis (2003).

[25] G. Li, X. Yang, G. Dai, CFD simulation of effects of the configuration of gas distributors on gas-liquid flow and mixing in a bubble column, Chemical Engineering Science 64 (2009) 5104–5116.

[26] B.C. Ong, P. Gupta, A. Youssef, M. Al-Dahhan, M.P. Dudukovic, Computed Tomographic Investigation of the Influence of Gas Sparger Design on Gas Holdup Distribution in a Bubble Column, Industrial & Engineering Chemistry Research 48 (2009) 58–68.

[27] M. Jamialahmadi, H. Müller-Steinhagen, Effect of alcohol, organic acid and potassium chloride concentration on bubble size, bubble rise velocity and gas hold-up in bubble columns, The Chemical Engineering Journal 50 (1992) 47–56.

[28] B.N. Thorat, A.V. Shevade, K.N. Bhilegaonkar, R.H. Aglawe, U.P. Veera, S.S. Thakre, A.B. Pandit, S.B. Sawant, J.B. Joshi, Effect of Sparger Design and Height to Diameter Ratio on Fractional Gas Hold-up in Bubble Columns, Chemical Engineering Research and Design 76 (1998) 823–834.

[29] M. Abraham, S.B. Sawant, Effect of sparger design on the hydrodynamics and mass transfer characteristics of a bubble column, Indian Chemical Engineer 31 (XXXI) (1989) 31–36.

[30] M.W. Haque, K.D.P. Nigam, J.B. Joshi, Optimum gas sparger design for bubble columns with a low height-to-diameter ratio, The Chemical Engineering Journal 33 (1986) 63–69

[31] I. Iliuta, F. Larachi, D. Desvigne, J. Anfray, N. Dromard, D. Schweich, Multicompartment hydrodynamic model for slurry bubble columns, Chemical Engineering Science 63 (2008) 3379–3399.

[32] P.M. Wilkinson, A.P. Spek, L.L. van Dierendonck, Design parameters estimation for scale-up of high-pressure bubble columns, AIChE Journal 38 (1992) 544–554.

[33] A.V. Kulkarni, J.B. Joshi, Design and selection of sparger for bubble column reactor. Part II: Optimum sparger type and design, Chemical Engineering Research and Design 89 (2011) 1986–1995.

[34] V. Michele, D.C. Hempel, Liquid flow and phase holdup measurement and CFD modeling for two-and three-phase bubble columns, Chemical Engineering Science 57 (2002) 1899–1908.

[35] K. Schügerl, J. Lücke, U. Oels, Bubble column bioreactors, Advances in Biochemical Engineering/Biotechnology 7 (1977) 1–84.

[36] K. Idogawa, K. Ikeda, T. Fukuda, S. Morooka, Formation and Flow of Gas Bubbles in a Pressurized Bubble Column with a Single Orifice or Nozzle Gas Distributor, Chemical Engineering Communications 59 (1987) 201–212.

[37] T. Miyahara, H. Terakado, T. Takahashi, Transition from Bubbling to Jetting at Single Orifices, Journal of Chemical Engineering of Japan 16 (1983) 454–458.

[38] F. Fischer, D. Hoppe, E. Schleicher, G. Mattausch, H. Flaske, R. Bartel, U. Hampel, An ultra fast electron beam x-ray tomography scanner, Measurement Science and Technology 19 (2008) (094002) 1–11.

[39] M. Banowski, D. Lucas, L. Szalinski, A new algorithm for segmentation of ultrafast X-ray tomographed gas-liquid flows, International Journal of Thermal Sciences 90 (2015) 311–322.

[40] Y.M. Lau, K. Müller, S. Azizi, M. Schubert, Voronoï analysis of bubbly flows via ultrafast X-ray tomographic imaging, Experiments in Fluids 57 (2016) (57:35) 1–12.

[41] N.A. Kazakis, A.A. Mouza, S.V. Paras, Experimental study of bubble formation at metal porous spargers: Effect of liquid properties and sparger characteristics on the initial bubble size distribution, Chemical Engineering Journal 137 (2008) 265–281.

[42] S.S. Rabha, V.V. Buwa, Experimental Investigations of Rise Behavior of Monodispersed/Polydispersed Bubbly Flows in Quiescent Liquids, Industrial & Engineering Chemistry Research 49 (2010) 10615–10626.

[43] W.-D. Deckwer, R. Burckhart, G. Zoll, Mixing and mass transfer in tall bubble columns, Chemical Engineering Science 29 (1974) 2177–2188.

[44] K.-H. Mangartz, T. Pilhofer, Untersuchungen zur Gasphasendispersion in Blasensäulenreaktoren, Verfahrenstechnik (Mainz) 14 (1980) 40–44.

[45] P.V. Danckwerts, Continuous flow systems, Chemical Engineering Science 2 (1953) 1–13.

[46] K. Akita, F. Yoshida, Bubble Size, Interfacial Area, and Liquid-Phase Mass Transfer Coefficient in Bubble Columns, Industrial & Engineering Chemistry Process Design and Development 13 (1974) 84–91.

[47] W.-D. Deckwer, I. Adler, A. Zaidi, A comprehensive study on CO2-interphase mass transfer in vertical cocurrent and countercurrent gas-liquid flow, The Canadian Journal of Chemical Engineering 56 (1978) 43–55.

[48] R. Wendt, Untersuchungen zum Wärmeübergang an Einzelrohren und Querangeströmten Rohrbündelwärmeaustauschern in Blasensäulenreaktoren, PhD Thesis Technische Universität Dortmund (1983).

[49] K. Akita, F. Yoshida, Gas Holdup and Volumetric Mass Transfer Coefficient in Bubble Columns. Effects of Liquid Properties, Industrial & Engineering Chemistry Process Design and Development 12 (1973) 76–80.

[50] H. Luo, H.F. Svendsen, Turbulent circulation in bubble columns from eddy viscosity distributions of single-phase pipe flow, The Canadian Journal of Chemical Engineering 69 (1991) 1389–1394.

[51] J.-M. Schweitzer, J. Bayle, T. Gauthier, Local gas hold-up measurements in fluidized bed and slurry bubble column, Chemical Engineering Science 56 (2001) 1103–1110.

[52] Y. Wu, B.C. Ong, M.H. Al-Dahhan, Predictions of radial gas holdup profiles in bubble column reactors, Chemical Engineering Science 56 (2001) 1207–1210.

[53] S. Nedeltchev, Theoretical prediction of mass transfer coefficients in both gas-liquid and slurry bubble columns, Chemical Engineering Science 157 (2017) 169–181.

[54] J. Kennedy, R. Eberhart, Particle swarm optimization, Neural Networks, 1995. Proceedings., IEEE International Conference on 4 (1995) 1942–948.

[55] J.F. Davidson, B.O.G. Schüler, Bubble formation at an orifice in a viscous liquid, Chemical Engineering Research and Design 75 (1997) S105–S115.

[56] E.S. Gaddis, A. Vogelpohl, Bubble formation in quiescent liquids under constant flow conditions, Chemical Engineering Science 41 (1986) 97–105.

[57] M. Jamialahmadi, M.R. Zehtaban, H. Müller-Steinhagen, A. Sarrafi, J.M. Smith, Fluid Flow Study of Bubble Formation Under Constant Flow Conditions, Chemical Engineering Research and Design 79 (2001) 523–532.

[58] R. Kumar, N.K. Kuloor, The Formation of Bubbles and Drops, Advances in Chemical Engineering 8 (1970) 255–368.

[59] A. Mersmann, Wann werden alle Löcher einer Siebboden-Lochplatte durchströmt?, Chemie Ingenieur Technik 35 (1963) 103–107.

[60] R.H.S. Winterson, A simple method of predicting bubble size in bubble columns, Chemical Engineering and Processing: Process Intensification 33 (1994) 1–5.

[61] H. Hikita, S. Asai, K. Tanigawa, K. Segawa, M. Kitao, Gas hold-up in bubble columns, The Chemical Engineering Journal 20 (1980) 59–67.

[62] G. Bloch, H..-J. Zander, B. Wunderlich, T. Acher, Axial and Radial Dispersion in a Large-Diameter Bubble Column Reactor at Low Height-to-Diameter Ratios, Chemie Ingenieur Technik 87 (2015) 756–761.